AJNR

Methionine PET Findings in the Diagnosis of Brain Tumors and Non-Tumorous Mass Lesions: A Single-Center Report on 426 Cases

Yoshiki Shiba, Kosuke Aoki, Fumiharu Ohka, Shoichi Deguchi, Junya Yamaguchi, Hiroki Shimizu, Sachi Maeda, Yuhei Takido, Ryo Yamamoto, Akihiro Nakamura and Ryuta Saito

AJNR Am J Neuroradiol published online 12 June 2025
http://www.ajnr.org/content/early/2025/06/11/ajnr.A8871

This information is current as of July 31, 2025.

Published June 12, 2025 as 10.3174/ajnr.A8871
This represents the accepted version of the manuscript and also includes the supplemental material; it differs from the final version of the article.

ORIGINAL RESEARCH

Methionine PET Findings in the Diagnosis of Brain Tumors and Non-Tumorous Mass Lesions: A Single-Center Report on 426 Cases

Yoshiki Shiba*, Kosuke Aoki*, Fumiharu Ohka, Shoichi Deguchi, Junya Yamaguchi, Hiroki Shimizu, Sachi Maeda, Yuhei Takido, Ryo Yamamoto, Akihiro Nakamura, and Ryuta Saito

ABSTRACT

BACKGROUND AND PURPOSE: Differentiating between a brain tumor and a non-tumorous lesion remains a significant diagnostic challenge, particularly when conventional imaging modalities such as CT and MRI provide inconclusive results. While MET-PET has shown potential in neuro-oncology, its diagnostic performance across a broad spectrum of brain pathologies has not been comprehensively evaluated. This study therefore assessed the sensitivity, specificity, and uptake patterns of MET-PET in a large cohort of brain lesions.

MATERIALS AND METHODS: This single-center retrospective study analyzed 426 consecutive patients with undiagnosed brain lesions who underwent MET-PET imaging between January 2019 and May 2024. TNRs were calculated using a threshold of 1.5 for positive findings. Histological diagnoses were established based on the World Health Organization 2021 criteria, IDH mutation status and 1p/19q-codeletion.

RESULTS: Among the cohort, 342 cases (67.8%) were confirmed as having tumorous lesions, 76 (17.8%) as having non-tumorous lesions, and 61 (14.3%) remained undiagnosed. MET-PET exhibited high sensitivity (86.2%) but limited specificity (47.4%) for tumor detection. In multiple sclerosis cases, MET-PET showed a remarkably high positivity rate (n = 10/12) that was significantly higher than for other non-tumorous lesions. In terms of tumors, IDH-wildtype glioblastomas had significantly higher TNRs compared to IDH-mutant gliomas, while oligodendrogliomas had higher TNRs compared to astrocytomas, in which TNR values correlated with tumor grade.

CONCLUSIONS: MET-PET demonstrated robust sensitivity for brain tumor detection, but was limited by low specificity due to false positives in inflammatory conditions and false negatives for low-grade tumors. These findings imply the importance of integrating MET-PET with other imaging modalities to enhance diagnostic accuracy.

ABBREVIATIONS: MET-PET = ^{11}C-methionine positron emission tomography; TNR = Tumor/normal region ratio; IDH = isocitrate dehydrogenase.

Received month day, year; accepted after revision month day, year.

From the Department of Neurosurgery, Nagoya University School of Medicine, Nagoya, Japan

The authors have no conflicts of interest to disclose.

Ryuta Saito, M.D., Ph.D.

Department of Neurosurgery, Nagoya University School of Medicine,

65 Tsurumai-cho, Showa-ku, Nagoya 466-8550, Japan.

Copyright 2025 by American Society of Neuroradiology.
Copyright 2025 by American Society of Neuroradiology.

Telephone: 81-52-744-2353; Fax: 81-52-744-2360

E-mail: saito.ryuta.b1@f.mail.nagoya-u.ac.jp

SUMMARY SECTION

PREVIOUS LITERATURE: Previous studies have demonstrated the utility of ^{11}C-methionine positron emission tomography (MET-PET) for diagnosing and evaluating brain tumors. MET-PET has shown high sensitivity in detecting gliomas, distinguishing tumor recurrence from radiation necrosis, and aiding in treatment planning. However, its specificity has been limited due to uptake by non-tumorous lesions. The diagnostic performance of MET-PET across diverse brain pathologies, particularly in light of the 2021 WHO classification of central nervous system tumors, has not been comprehensively evaluated. Additionally, the lack of standardization in MET-PET protocols and quantitative measures across studies has made it challenging to compare results.

KEY FINDINGS: This study of 426 cases found that MET-PET had high sensitivity (86.2%) but limited specificity (47.4%) for brain tumor detection. In cases of multiple sclerosis, MET-PET demonstrated a high positivity rate. Among tumors, glioblastomas had significantly higher TNRs compared to IDH-mutant gliomas, while oligodendrogliomas exhibited higher TNRs compared to astrocytomas.

KNOWLEDGE ADVANCEMENT: This study provides valuable insights into MET-PET's diagnostic performance across various brain pathologies. The findings highlight the necessity of integrating MET-PET with other imaging modalities to improve diagnostic accuracy. Additionally, they emphasize the importance of establishing standardized protocols, which will aid in enhancing the utility of MET-PET in clinical practice.

INTRODUCTION

Accurate diagnosis and evaluation of brain tumors pose significant clinical challenges. Conventional imaging modalities, such as magnetic resonance imaging (MRI) and computed tomography (CT), primarily provide structural information but often fall short in clearly distinguishing viable tumor tissue from non-neoplastic changes. Consequently, advanced metabolic imaging techniques, particularly positron emission tomography (PET), have been increasingly explored to improve diagnostic accuracy and inform clinical decision-making.

^{11}C-methionine PET (MET–PET) is a specialized imaging modality that has demonstrated considerable utility in the diagnosis and evaluation of brain tumors [1–4]. This technique uses ^{11}C-methionine, an amino acid tracer that is preferentially taken up by actively proliferating tumor cells. A key advantage of MET–PET is its low background uptake by normal brain tissue, which allows enhanced differentiation of neoplastic activity [5]. A principal application of MET–PET is the detection of gliomas and other intracranial tumors [6,7]. The technique is effective in identifying both low- and high-grade gliomas, with higher-grade tumors typically exhibiting greater MET uptake [6,8]. This feature is essential, not only for initial tumor detection but also for differentiating between tumor recurrence and radiation-induced necrosis [9].

MET–PET has demonstrated significantly higher sensitivity (97%) in the detection of recurrent brain tumors compared to fluorodeoxyglucose PET (48%) [5]. This enhanced sensitivity is particularly valuable in pediatric high-grade gliomas, where MET–PET has achieved 100% sensitivity and 93% accuracy in predicting tumor recurrence, surpassing the diagnostic performance of conventional MRI [10]. Additionally, MET–PET plays critical roles in treatment planning and monitoring [11]. By precisely delineating tumor extent, it assists in surgical planning and radiotherapy targeting [12]. Changes in MET uptake over time can also serve as biomarkers for tumor progression or therapeutic response [7].

Beyond gliomas, MET–PET is effective in visualizing metastatic brain lesions and aids in differentiating primary from secondary brain tumors [13]. Overall, MET–PET provides valuable metabolic information that complements structural imaging, thereby improving diagnostic precision and contributing to better clinical outcomes in patients with suspected or confirmed brain tumors [14].

However, increased MET uptake is not exclusive to neoplastic processes, and false-positive results may occur if findings are not carefully interpreted. Non-neoplastic conditions that can exhibit elevated MET uptake include:

1. Inflammatory lesions: Conditions such as tumefactive demyelinating disease can result in increased MET uptake, mimicking malignant neoplasms. This uptake is likely attributable to enhanced amino acid transport and metabolism in activated inflammatory cells [15–17].

2. Hematomas: Some hematomas demonstrate increased MET accumulation, which may be misinterpreted as tumor activity [18].

3. Infarctions: Elevated MET uptake in infarcted areas is associated with inflammatory cell infiltration and gliosis. Breakdown of the blood-brain barrier allows MET to leak into the extracellular space, and altered amino acid transport further contributes to its uptake [18].

4. Infections: Brain abscesses may exhibit MET accumulation due to both blood-brain barrier (BBB) disruption and the high density of infiltrating inflammatory cells [18].

5. Radiation necrosis: This post-treatment complication may show mild to moderate MET uptake that is typically lower than that seen in recurrent tumors. Quantitative assessments using tumor-to-normal region ratios can aid in distinguishing between necrosis and true recurrence [19–21].

6. Inflammatory conditions: Conditions such as idiopathic hypertrophic pachymeningitis have demonstrated increased MET uptake, which may be valuable for assessing disease activity [5].

While the diagnostic benefits and limitations of MET–PET have been reported in previous studies, few investigations have involved large-scale examinations conducted under a standardized protocol. Moreover, detailed evaluations of MET–PET's diagnostic performance, including methionine uptake patterns across different tumor histologies and findings in non-neoplastic conditions, remain limited. This study aimed to address this gap by analyzing MET uptake across a broad spectrum of brain tumors and non-tumorous lesions. By doing so, the study sought to identify the tumor types most amenable to MET–PET evaluation and to clarify the method's potential diagnostic pitfalls. This comprehensive approach is expected to yield a more refined understanding of MET–PET's clinical utility and support its optimized application in neuro-oncologic imaging.

MATERIALS AND METHODS

Study Design and Patient Population

This section may be divided into subsections if it facilitates reading the paper. The research design, patients/subjects, material used, means of confirming diagnoses, and statistical methods should be included. Do not include manufacturer's names unless the specific product is important to the procedures performed. When appropriate, indicate that approval was obtained from the institution's review board. Indicate that informed consent has been obtained from patients who participated in clinical investigations.

In animal experimentation, acknowledge that National Institutes of Health or equivalent guidelines were followed. If there is a sponsoring company, include at the end of this section what input that company had in the formulation of the paper.

MET-PET Image Acquisition and Data Analysis

All MET–PET scans were performed using a Biograph Vision 600 PET/CT scanner (Siemens Healthineers, Erlangen, Germany) with integrated 64-slice multidetector CT. Patients fasted for at least 3 hours prior to the scan and received an intravenous injection of 370 MBq of MET. Ten minutes after injection, a low-dose, non-contrast-enhanced head CT was acquired for attenuation correction, followed by a 20-minute 3D emission scan in a single bed position.

PET images were reconstructed using the Ordered Subset Expectation Maximization algorithm with time-of-flight technology. MET uptake was quantified using the standardized uptake value (SUV), calculated as:

SUV = tissue activity [Bq]/tissue volume [mL])/(injected radioisotope activity [Bq]/body weight [g]. Tumor uptake was expressed as the tumor-to-normal region ratio (TNR), defined as the maximum SUV of the tumor divided by the mean SUV of the normal region [23]. Normal control values were obtained by averaging three 1-cm circular regions of interest (ROIs) placed on the contralateral frontal cortex (Figure 1A). Tumor ROI placement was reviewed and verified by two neurosurgeons and two radiological technologists to minimize interobserver variability. For cases with inconspicuous lesions on PET, co-registration with MRI was performed to localize the tumor. The metabolic tumor volume (MTV) was defined as the volume of tissue with a TNR $\geq$ 1.5.

Histological Analysis and Diagnosis

Patients diagnosed with tumors underwent either surgical resection or biopsy for histopathological confirmation. Surgical strategy aimed for maximal safe resection in all applicable cases. However, in select patients, only biopsy was feasible due to anatomical constraints, such as tumor location in deep brain structures (e.g., thalamus), involvement of eloquent cortical areas, or a combination of these factors. Overall, 81.9% of patients underwent total or subtotal resection, while 18.9% underwent biopsy.

All lesions were classified according to the 2021 WHO classification of CNS tumors [22]. Isocitrate dehydrogenase (IDH) mutation status was assessed via immunohistochemistry for IDH1 p.R132H and, when necessary, by direct Sanger sequencing to detect additional IDH1 and IDH2 variants. The 1p/19q codeletion was evaluated using multiplex ligation-dependent probe amplification [24–26].

Non-neoplastic lesions were diagnosed according to the respective disease-specific diagnostic criteria. For example, multiple sclerosis (MS) was diagnosed based on MRI findings in conjunction with cerebrospinal fluid analysis showing oligoclonal IgG bands or an elevated IgG index, as well as serological detection of disease-specific antibodies. Cortical malformations were confirmed by histological examination of biopsy specimens, while vascular malformations were identified via angiographic studies.

Determination of Optimal TNR Cut-Off values Between Tumor Groups Using ROC Analysis

To determine the optimal cut-off TNR values for differentiating between tumor groups, receiver operating characteristic (ROC) curve analysis was employed. For each pairwise comparison of tumor types, the TNR was used as the continuous variable, and diagnoses were binarized accordingly. The optimal diagnostic thresholds were determined using the Youden Index, which maximizes the value of (sensitivity + specificity − 1). Sensitivity, specificity, and the area under the curve (AUC) were calculated, and 95% confidence intervals for the AUC were derived using the DeLong method.

Statistical Analysis

All statistical analyses were conducted using R software (version 4.2.1). The "ggplot2" (version 3.5.1) and "plyr" (version 1.8.9) packages were used for data visualization and manipulation. Differences in PET positivity rates among disease groups were evaluated using Fisher's exact test. To visualize the distribution of TNR values, box plots were constructed displaying the median, interquartile range, and minimum and maximum values. Outliers, defined as data points exceeding 1.5 times the interquartile range from the quartiles, were plotted as individual points. Groupwise differences in TNR values between tumor types were assessed using the Wilcoxon rank-sum test.

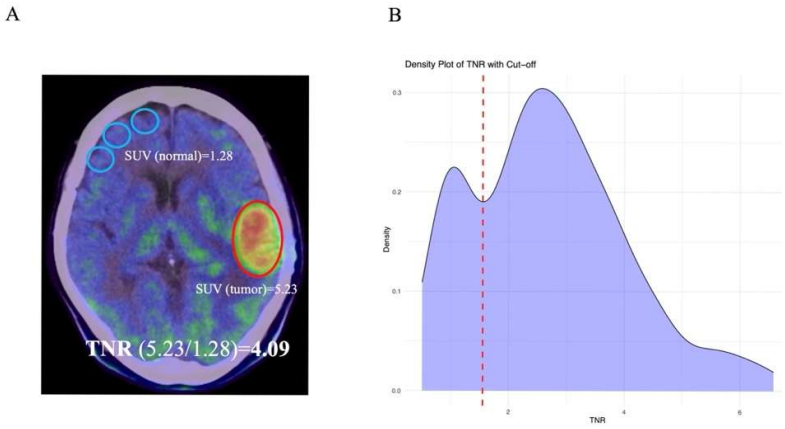

FIG 1. Representative example of 11C-methionine (MET)–positron emission tomography (PET) image for calculating tumor-to-normal region ratio (TNR) and distribution of TNR in diagnosed cases

(A) The blue circles indicate regions of interest (ROIs) for normal tissue and red outline indicates ROI for tumor. The average standardized uptake value (SUV) of normal tissue is 1.28, and the maximum SUV of the tumor is 5.23. The TNR can be calculated by dividing 5.23 by 1.28, resulting in a TNR of 4.09.

(B) Density plot of TNR for all confirmed diagnosis cases with cut-off

RESULTS

Patient Characteristics

In total, 426 patients were analyzed, and their clinical characteristics are summarized in Table 1. The median follow-up duration was 43 months (range, 1.1–63.1 months). Among the patients, 235 (55.2%) were male and 191 (44.8%) were female. The mean age at diagnosis was 45.1 years (range, 2 months to 83 years). The cohort included 289 tumors (67.8%), 76 non-tumorous lesions (17.8%), and 61 cases (14.3%) in which biopsy was not performed and alternative diagnostic tests did not yield a definitive diagnosis. The undiagnosed cases were neither surgically excised nor biopsied. Given the absence of symptom progression and that no radiological changes were observed during follow-up MRI examinations, a clinical decision was made to continue observation.

The tumor group included 54 cases of glioblastoma, IDH-wild type (IDHwt-GBM); 41 cases of astrocytoma, IDH-mutant, CNS WHO grade 2 (IDHm-A2); 16 cases of astrocytoma, IDH-mutant, CNS WHO grade 3 (IDHm-A3); 4 cases of astrocytoma, IDH-mutant, CNS WHO grade 4 (IDHm-A4); 37 cases of oligodendroglioma, IDH-mutant and 1p/19q-codeleted, CNS WHO grade 2 (IDHm-O2); 16 cases of oligodendroglioma, IDH-mutant and 1p/19q-codeleted, CNS WHO grade 3 (IDHm-O3); 19 pediatric-type diffuse high-grade gliomas; 11 pilocytic astrocytomas (PAs); 15 cases of primary central nervous system lymphoma (PCNSL); 8 ependymal tumors; 7 germ cell tumors; 11 meningiomas; 12 metastatic brain tumors; and 42 cases of other brain tumors. Among the metastatic brain tumors, the primary sites were the lung in 7 cases and the breast in 5 cases. The non-tumorous lesions included 12 cases of MS, 7 of other demyelinating diseases, 13 of cortical dysplasia, 15 of autoimmune diseases, 9 of vascular malformations, and 20 classified as 'other' (Supplementary Table).

Diagnostic Yield of MET-PET for Tumors and Non-Tumorous Lesions

An AUC analysis of TNRs was conducted for all cases with a confirmed diagnosis to determine the optimal cutoff value, resulting in a threshold of 1.55 (Figure 1B). Based on this analysis, TNR values of 1.5 or higher were considered MET–PET positive, while values below 1.5 were considered MET–PET negative. In cases where PET imaging failed to clearly visualize the lesion, image registration with MRI was used, and the lesion was classified as PET-negative if the TNR of the affected area was below 1.5.

Among the 289 tumor cases, MET–PET yielded positive results in 249 cases, while it was positive in 40 of the 76 non-tumorous lesions, indicating a statistically significant difference (sensitivity: 86.2%, specificity: 47.4%, $p < 0.001$) (Table 2). Although MET–PET demonstrated high sensitivity, its specificity was limited. Notably, some tumors showed no MET uptake, and conversely, several non-tumorous lesions exhibited MET uptake. This phenomenon was particularly prominent in cases of MS, where MET–PET showed a remarkably high positivity rate, being positive in 10 out of 12 cases (Table 3). This rate was significantly higher than that observed in non-tumorous lesions excluding MS, of which 30 out of 64 were MET–PET positive ($p < 0.05$), and it did not significantly differ from the overall tumor positivity rate ($p = 0.3$) (Figure 2).

Representative examples of non-tumorous lesions with MET uptake are shown in Figure 3. Figures 3A–F depict a case of MS. MRI fluid-attenuated inversion recovery (FLAIR) imaging showed high signal intensity in the left corona radiata with partial contrast enhancement, initially implying a tumor. This region exhibited MET uptake (TNR: 2.26). In contrast, another area around the left cerebral ventricle also demonstrated a high FLAIR signal, but lacked enhancement and showed no MET uptake (TNR: 0.92). The diagnosis of MS was confirmed by cerebrospinal fluid and serological examinations, and the lesions resolved following steroid pulse therapy. Figures 3G–J illustrate a case of dural arteriovenous fistula (dAVF). The lesion showed contrast enhancement on MRI and MET uptake (TNR: 2.87). Following treatment with transcatheter arterial embolization, MET–PET became negative.

MET Uptake Rate in Each Tumor

We evaluated TNR values across various brain tumor categories (Figure 4). Brain tumors were broadly classified into adult-type and pediatric-type groups, with no significant difference between the two in the overall MET–PET positivity rates ($p = 0.793$). Focusing on adult-type tumors, glioneuronal tumors demonstrated a significantly lower MET–PET positivity rate ($p < 0.05$) (Table 4).

A detailed analysis was conducted of diffuse gliomas, which represented the largest subgroup in this study (Figure 5A). Among these, IDHwt-GBM exhibited markedly higher TNR values compared to IDHm-gliomas ($p < 0.001$) (Figure 5B). Within the IDHm-glioma group, oligodendrogliomas consistently showed higher TNR values than astrocytomas ($p < 0.001$) (Figure 5C). TNRs did not vary significantly across WHO grades in oligodendrogliomas ($p = 0.51$), whereas astrocytomas demonstrated a progressive increase in MET uptake in higher grades (Figure 5D). A significant distinction was observed between IDHm-A2 and their higher-grade counterparts, implying a metabolic shift during tumor progression ($p < 0.001$). Of the 41 IDHm-A2 cases, 24 were MET–PET negative.

In the pediatric-type tumor group, diffuse intrinsic pontine glioma exhibited significantly higher TNR values compared to PA ($p < 0.05$) (Figure 6A). Meanwhile, all metastatic brain tumors in the current cohort demonstrated positive MET–PET findings. However, their TNR values were significantly lower than those observed in IDHwt-GBM and PCNSL (Figure 6B).

ROC curve analyses were performed to determine the optimal TNR cutoff values for differential diagnosis (Figures 5, 6). For instance, a TNR cutoff of 2.78 effectively distinguished IDHm-glioma from IDHwt-GBM, with a sensitivity of 0.93 and a specificity of 0.63.

To assess MET uptake further, we analyzed MTV as a volumetric parameter alongside TNRs. MTV values were elevated in IDHwt-GBM, showed a positive correlation with increasing grade in astrocytomas, and remained independent of grade in oligodendrogliomas, paralleling the trends observed with TNRs (Figure 7).

Representative clinical cases are shown in Figure 8. Figures 8A and B illustrate a case with high T2 signal intensity in the left temporal lobe on MRI, yet a negative MET–PET finding; the pathological diagnosis was IDHm-A2. In contrast, Figures 8C–E depict a brainstem lesion with non-enhancing T2 hyperintensity on MRI, initially suggestive of a circumscribed lesion such as PA. However, MET–PET revealed a high SUV of 4.85, indicating potential malignancy. Biopsy confirmed the lesion to be a diffuse midline glioma.

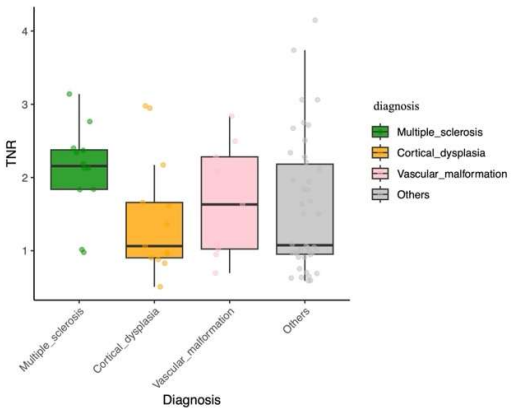

FIG 2. Tumor-to-normal region ratio (TNR) in non-tumorous lesion

Each dot represents the TNR value for an individual patient. The box plot summarizes the distribution of these values. The bottom and top edges of the box represent the 25th (Q1) and 75th (Q3) percentiles, respectively, with the line inside the box indicating

the median. The whiskers extend to the smallest and largest values within 1.5 times the interquartile range (IQR) from Q1 and Q3. Values outside this range are considered outliers.

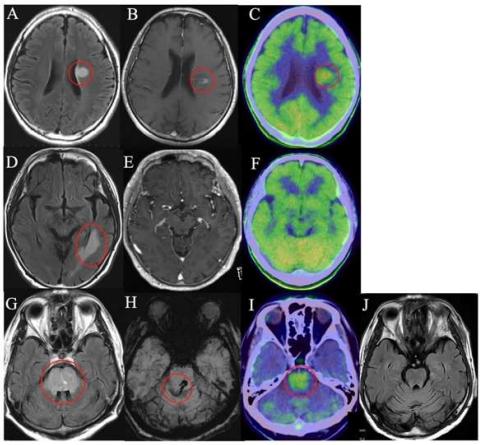

FIG 3. Non-neoplastic lesions exhibiting elevated 11C-methionine (MET) uptake

(A)- (F) A case of multiple sclerosis (MS) in a 59-year-old patient presenting with right hemiparesis of the upper and lower limbs

Figure (A)-(C) show images of active MS lesion, while Figure (D)-(F) show images of inactive MS lesion. This case improved with steroid pulse therapy.

(A) Axial magnetic resonance imaging (MRI) fluid attenuated inversion recovery (FLAIR) demonstrates high-signal lesion in the left corona radiata (circle).

(B) Axial MRI postcontrast T1-weighted image demonstrates contrast enhancement in part of the high-signal area on FLAIR (circle).

(C) Axial fused MET–positron emission tomography (PET) /Computed Tomography (CT) demonstrates increased MET uptake in part of the high-signal area on FLAIR (circle).

(D) Axial MRI FLAIR demonstrates high-signal lesion in the left temporal lobe (circle).

(E) Axial MRI postcontrast T1-weighted image demonstrates no contrast enhancement in the lesion of the left temporal lobe.

(F) Axial fused MET–PET/CT demonstrates no increased MET uptake in the lesion of the left temporal lobe.

(G)-(J) A case of dural arteriovenous fistula (dAVF) in a 49-year-old patient presenting with gait disorder

This case was initially suspected to be a tumor, but was diagnosed as dAVF by angiography and treated with transvenous coil embolization

(G) Axial MRI FLAIR demonstrates high-signal lesion in the pons (circle).

(H) Axial MRI susceptibility-Weighted Imaging (SWI) demonstrates a dilated vein in the pons (circle).

(I) Axial fused MET–PET/CT demonstrates increased MET uptake in part of the high-signal area on FLAIR, therefore a tumor was initially suspected (circle).

(J) Axial MRI FLAIR indicates that the high signal disappeared after transvenous coil embolization.

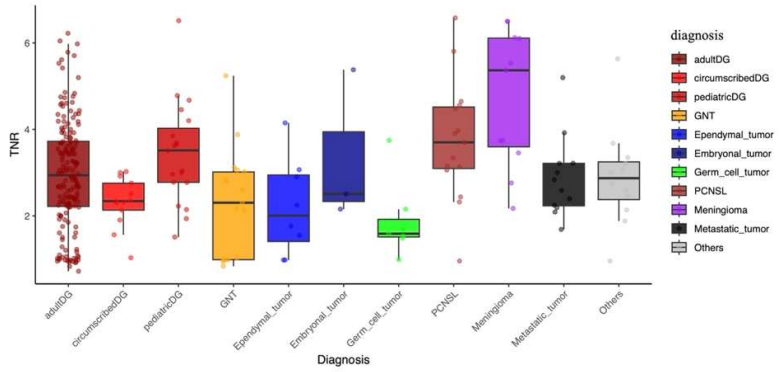

FIG 4. Tumor-to-normal region ratio (TNR) in each tumor type

Each dot represents the TNR value for an individual patient. The box plot summarizes the distribution of these values. The bottom and top edges of the box represent the 25th (Q1) and 75th (Q3) percentiles, respectively, with the line inside the box indicating the median. The whiskers extend to the smallest and largest values within 1.5 times the interquartile range (IQR) from Q1 and Q3. Values outside this range are considered outliers.

DG, Diffuse glioma; GNT, glioneural tumor; PCNSL, Primary central nervous system lymphoma

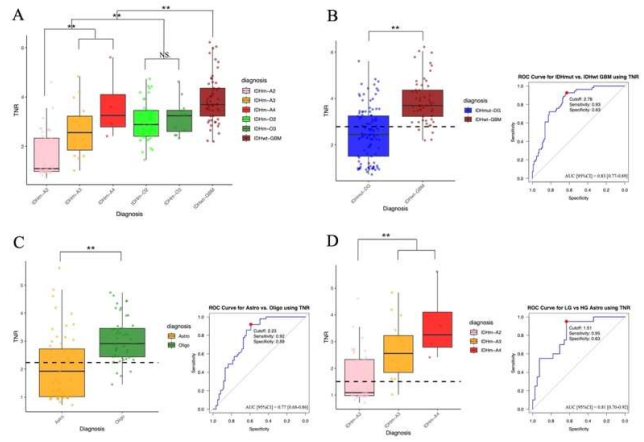

FIG 5. Analysis of tumor-to-normal region ratio (TNR) differences by glioma classification

(A) TNR in adult diffuse glioma

(B) TNR in isocitrate dehydrogenase (IDH)-wild type and IDH-mutant glioma

(C) TNR in astrocytoma and oligodendroglioma

(D) TNR in astrocytoma

Panels A, B, C, and D each show, on the left, a bee swarm plot overlaid with a box plot illustrating the distribution of TNR for each diagnostic group. The bottom and top edges of the box represent the 25th (Q1) and 75th (Q3) percentiles, respectively, with the line inside the box indicating the median. The whiskers extend to the smallest and largest values within 1.5 times the

interquartile range (IQR) from Q1 and Q3. Values outside this range are considered outliers. The horizontal dashed line indicates the optimal cutoff value for TNR. On the right of panels B, C, and D, receiver operating characteristic (ROC) curves are displayed. The red dot on each ROC curve marks the optimal cutoff point, at which the corresponding sensitivity and specificity values are indicated. The area under the ROC curve (AUC) is shown together with its 95% confidence interval.

**, p<0.001; NS, Not significant; IDHm-A2, Astrocytoma, IDH-mutant, CNS WHO grade 2; IDHm-A3, Astrocytoma, IDH-mutant, CNS WHO grade 3; IDHm-A4, Astrocytoma, IDH-mutant, CNS WHO grade 4; IDHm-O2, Oligodendroglioma, IDH-mutant and 1p/19q-codeleted, CNS WHO grade 2; IDHm-O3, Oligodendroglioma, IDH-mutant and 1p/19q-codeleted, CNS WHO grade 3; IDHwt-GBM, Glioblastoma, IDH-wild type

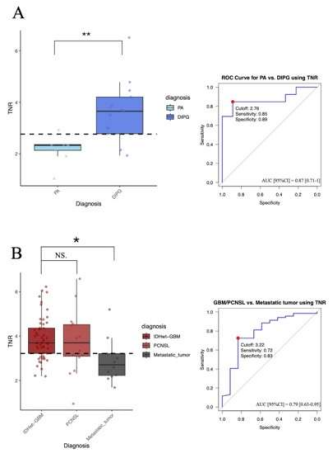

FIG 6. Comparative analysis of tumor-to-normal region ratio (TNR) across tumor types

(A) TNR in pilocytic astrocytoma (PA) and diffuse intrinsic pontine glioma (DIPG)

(B) TNR in glioblastoma, isocitrate dehydrogenase (IDH)-wild type, primary central nervous system lymphoma (PCNSL) and metastatic tumor

Panels A and B each show, on the left, a bee swarm plot overlaid with a box plot illustrating the distribution of TNR for each diagnostic group. The bottom and top edges of the box represent the 25th (Q1) and 75th (Q3) percentiles, respectively, with the line inside the box indicating the median. The whiskers extend to the smallest and largest values within 1.5 times the interquartile range (IQR) from Q1 and Q3. Values outside this range are considered outliers. The horizontal dashed line indicates the optimal cutoff value for TNR. On the right of panels A and B, receiver operating characteristic (ROC) curves are displayed. The red dot on each ROC curve marks the optimal cutoff point, at which the corresponding sensitivity and specificity values are indicated. The area under the ROC curve (AUC) is shown together with its 95% confidence interval.

**, p<0.001; *, p<0.05; NS, Not significant

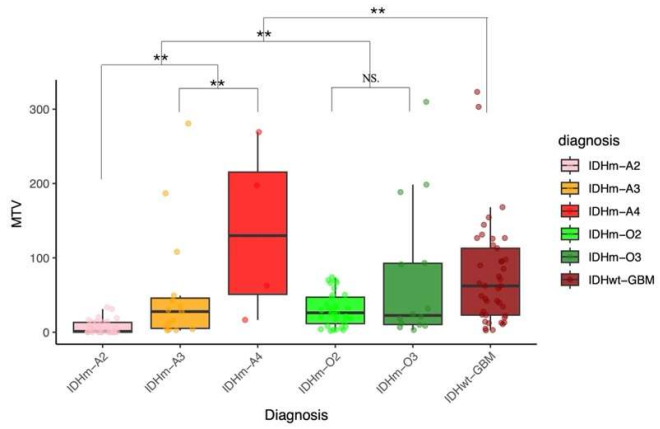

FIG 7. Metabolic tumor volume in tumor

Each dot represents the tumor-to-normal region ratio (TNR) value for an individual patient. The box plot summarizes the distribution of these values. The bottom and top edges of the box represent the 25th (Q1) and 75th (Q3) percentiles, respectively, with the line inside the box indicating the median. The whiskers extend to the smallest and largest values within 1.5 times the interquartile range (IQR) from Q1 and Q3. Values outside this range are considered outliers.

MTV, metabolic tumor volume; **, p<0.001; NS, Not significant; IDHm-A2, Astrocytoma, IDH-mutant, CNS WHO grade 2; IDHm-A3, Astrocytoma, IDH-mutant, CNS WHO grade 3; IDHm-A4, Astrocytoma, IDH-mutant, CNS WHO grade 4; IDHm-O2, Oligodendroglioma, IDH-mutant and 1p/19q-codeleted, CNS WHO grade 2; IDHm-O3, Oligodendroglioma, IDH-mutant and 1p/19q-codeleted, CNS WHO grade 3; IDHwt-GBM, Glioblastoma, IDH-wild type

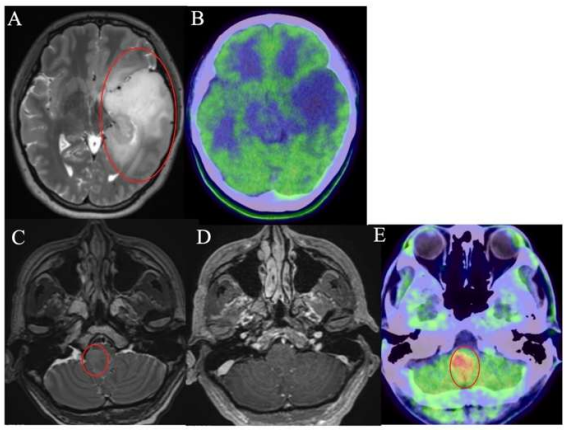

FIG 8. Clinical presentation of 11C-methionine (MET)–positron emission tomography (PET) in neoplastic lesions

(A)-(B) A case of astrocytoma, IDH-mutant, CNS WHO grade 2 (IDHm-A2) in a 35-year-old patient presenting with **epilepsy**

The patient was diagnosed with IDHm-A2 by pathological examination following resection via craniotomy.

(A) Axial magnetic resonance imaging (MRI) T2-weighted image demonstrates high-signal lesion in the left temporal lobe (circle).

(B) Axial fused 11C-methionine (MET)–positron emission tomography (PET)/Computed Tomography (CT) demonstrates no

increased MET uptake in the lesion of the left temporal lobe.

(C)- (E) A case of diffuse midline glioma in a 61-year-old patient presenting with **right upper limb paralysis**

Initial MRI findings were indicative of a low-grade tumor, like pilocytic astrocytoma, but MET–PET demonstrated a high tumor-to-normal region ratio (TNR), and pathological examination of the biopsy established the diagnosis of diffuse midline glioma.

(C) Axial MRI T2-weighted image demonstrates high-signal lesion in the pons (circle).

(D) Axial MRI postcontrast T1-weighted image demonstrates no apparent contrast enhancement in the lesion of the pons.

(E) Axial fused MET–PET/CT demonstrates increased MET uptake in the lesion of the pons (circle). A biopsy was performed, leading to a diagnosis of diffuse midline glioma.

DISCUSSION

In this study, we analyzed 426 cases that underwent MET–PET at our facility. Among the tumor types, IDHwt-GBM and IDHm-A2 were the most prevalent, although a wide range of other brain tumors were also identified. MET uptake patterns in brain tumors exhibited significant variations across different types and grades. IDHwt-GBM showed high MET uptake, with IDHwt-GBM demonstrating higher TNRs compared to IDHm-gliomas. This stark contrast highlights the aggressive nature of IDHwt-GBM and its distinct metabolic profile. This aggressiveness may partly be attributed to the BBB destruction due to high-grade malignancies, which could have contributed to the elevated MET uptake observed in IDHwt-GBM.

Furthermore, astrocytomas exhibited a tendency for increased MET uptake as their grade increased. In contrast, oligodendrogliomas showed high MET uptake irrespective of grade. This implies that oligodendrogliomas may possess a unique metabolic signature that differentiates them from astrocytomas. A distinguishing feature of oligodendrogliomas is their chicken-wire vascular structure, which is thought to contribute to increased cerebral blood volume and MET uptake [27]. Additionally, when comparing MET–PET results for gliomas of IDHwt-GBM and metastatic brain tumors, it was evident that TNRs tended to be higher in IDHwt-GBM. Previous reports have compared these two tumor types following radiation therapy [13], but the results of this study implied a difference between them even from the initial diagnosis.

Although MET–PET scans are a valuable tool for brain tumor diagnosis, they sometimes yield false negative results due to various factors. In our study, 40 out of 289 tumor cases resulted in negative MET–PET findings. More than half of the IDH-A2 cases were MET–PET negative. This was consistent with the known low cerebral blood volume of IDHm-A2 tumors, which may explain the negative MET–PET findings in these cases [27]. Several other factors may contribute to negative MET–PET results in tumor lesions. One such factor is the size of the lesion; very small tumors may not accumulate enough tracer to be detected [28]. In our study, however, all lesions were 10 mm or larger, which is a size that can typically be identified on MET–PET. Another potential factor is patient-specific variables, such as fasting status or medications, which can influence tracer distribution. In this study, all patients fasted for 4 hours prior to the examination and avoided drinks containing amino acids. A third factor is that brain tumors with significant edema or those predominantly composed of cysts may exhibit reduced MET uptake. The use of volumetric parameters such as metabolic tumor volume in this study revealed that tumors of these types generally had lower values.

When focusing on non-tumor lesions, MET–PET can show positive uptake, potentially mimicking brain tumors. Past reports have included examples, such as inflammatory conditions like MS and sarcoidosis, demyelinating diseases, cerebral infarctions, brain abscesses, radiation-induced necrosis, intracerebral hematomas, and areas associated with seizure activity [29–31]. In our study, more than half of the non-tumor cases were positive for MET–PET. For MS, the positivity rate of MET–PET was comparable to that of tumors overall. The uptake of MET was found to align with the contrast-enhanced regions in MRI. Contrast enhancement and the presence of neurological symptoms in these patients indicated that the MS lesions were active. MET–PET positivity in MS may be attributable to the infiltration and proliferation of inflammatory cells, such as T cells, as well as the disruption of the BBB, implying MS activity [16]. In this study, several cases with vascular disorders also had positive MET–PET results. Among the five cases that were MET–PET positive, two were dAVFs, and three were venous malformations. All of these cases exhibited lesions that were enhanced on MRI, initially implying tumors. The observed increase in MET uptake in vascular disorders, such as dAVF, may be attributed to BBB disruption caused by venous congestion and gliotic reactions involving the increased synthesis of intermediate filament proteins [32,33].

In addition to the biological characteristics, the discrepancies observed in diagnosis may be attributed to the lack of uniformity in MET–PET methodologies. The absence of standardized protocols is a significant issue, with scan initiation times after MET injection varying widely across studies, ranging from 5 to 30 minutes [34,35]. This lack of standardization can lead to inconsistencies in results and their interpretation. In our study, using the same protocol within a single facility ensured that trial conditions and procedures were consistently managed. This standardization of data collection and interpretation is believed to reduce errors and inconsistencies.

Another challenge lies in the variability of quantitative measures used in MET–PET analysis. Different studies have employed various quantitative indices, such as SUV mean, SUV max, and TNRs [35], making it difficult to compare results across studies [8,36]. In our

study, in addition to TNRs, which are commonly used in many reports, we also utilized volumetric indicators for evaluation. Although the thresholds for TNR values vary across different studies, we conducted a large number of PET scans and determined appropriate thresholds based on ROC curves. Additionally, the influence of plasma amino acid concentrations is a concern, as the concentrations of neutral amino acids in plasma can potentially affect MET uptake by tissues [37].

This study was a large-scale analysis conducted at a single institution, which ensured a high degree of consistency in its testing procedures and result interpretation. This consistency greatly improved the reliability and comparability of the data and significantly enhanced the academic value of the study. The single-site implementation allowed standardization of protocols and eliminated potential biases due to inter-institutional differences. Furthermore, the large sample size provided improved statistical power and more precise analysis. An important aspect of this study was its adherence to the latest WHO classification system while examining a considerably large sample. The study's compliance with the most recent WHO classification, combined with its extensive scale, enabled a comprehensive and up-to-date examination of the subject matter. Considering these factors, this study makes an important contribution to the field, providing valuable insights that could advance our understanding of the disease and contribute to the development of new treatment strategies.

However, this study had several limitations that warrant consideration. First, the retrospective nature of this study, in which data collection and analysis were based on historical records, introduced potential biases and the possibility of missing data. This study design inherently limits causal inference compared to prospective studies. Second, the criteria used for determining positive and negative PET scan results were unique to this study. These non-standardized criteria may differ from those widely adopted in other research institutions or clinical settings, potentially limiting the generalizability of our findings and complicating direct comparisons with other studies. Third, the amino acid PET tracer used in this study was limited to MET. O-(2-[18F]-fluoroethyl)-L-tyrosine (FET)–PET is an alternative PET tracer that has shown sensitivity and specificity comparable to MET–PET in the diagnosis of brain gliomas and metastases [29]. FET-PET has the potential to widely replace short-lived amino acid tracers like MET in many facilities. However, MET–PET has historically been used, resulting in the accumulation of extensive clinical data and widespread recognition of its effectiveness. Further comparisons and studies are needed to accumulate data on both tracers. Lastly, the inclusion of cases without definitive diagnoses in our cohort represents a significant limitation. The presence of undiagnosed cases introduces uncertainty in the interpretation of our results, particularly in assessing PET scan diagnostic accuracy.

Table 1: Clinical characteristics of patients (N=426)

Diagnosis	N (%)	Sex (M/F), %	Age at diagnosis, years Median [range]
Tumor	289 (67.8)	55.5/44.5	44.9 [2-83]
Astrocytoma, IDH-mutant, CNS WHO grade 2	41 (9.6)	56.4/43.6	49.1 [15-81]
Astrocytoma, IDH-mutant, CNS WHO grade 3	16 (3.8)	46.7/53.3	44.5 [26-83]
Astrocytoma, IDH-mutant, CNS WHO grade 4	4 (0.9)	25.0/75.0	33.5 [31-57]
Oligodendroglioma, IDH-mutant and 1p/19q-codeleted, CNS WHO grade 2	37 (8.7)	52.9/47.1	43.5 [20-62]
Oligodendroglioma, IDH-mutant and 1p/19q-codeleted, CNS WHO grade 3	12 (2.8)	50.0/50.0	42.9 [27-68]
Glioblastoma, IDH-wild type	54 (12.7)	53.0/47.0	54.7 [18-81]
Pediatric type diffuse high-grade glioma	19 (4.5)	50.0/50.0	8.5 [4-23]
Pilocytic astrocytoma	11 (2.6)	42.9/57.1	14.4 [11-73]
Ependymal tumor	8 (1.9)	40.0/60.0	27 [14-68]
Germ cell tumor	7 (1.6)	61.1/38.9	7.4 [6-26]
Primary central nervous system lymphoma	15 (3.5)	64.3/35.7	71.4 [47-83]
Meningioma	11 (2.6)	45.5/55.5	67.2 [38-76]
Metastatic tumor	12 (2.8)	30.0/70.0	69.9 [52-76]
Other	42 (9.9)	47.2/52.8	35.2 [2-70]
Non-tumorous lesions	76 (17.8)	48.7/51.3	35.8 [0-80]
Multiple sclerosis	12 (2.8)	40.0/60.0	32.6 [22-59]
Other demyelinating disease	7 (1.6)	42.9/57.1	31.4 [14-57]
Cortical dysplasia	13 (3.1)	57.1/42.9	17.4 [0-41]

Autoimmune disease	15 (3.5)	54.5/45.5	46.2 [8-66]
Vascular malformation	9 (2.1)	57.1/42.9	40.2 [17-46]
Others	20 (4.7)	43.8/56.2	41.4 [26-80]
Undiagnosed	61 (14.3)	52.5/47.5	51.7 [1-76]

Abbreviation: CNS, Central nervous system; WHO, World health organization; IDH, Isocitrate dehydrogenase

Table 2: Diagnostic yield of methionine PET

TNR>1.5	249	40	289
TNR<1.5	40	36	76
Total	289	76	
	Sensitivity:86.2%	Specificity:47.4%	

Abbreviation: PET, Positron emission tomography

Table 3: Methionine PET positive and negative for each non-tumorous lesion

Multiple sclerosis	10 (83.3%)	2 (16.7%)	0.027*
Cortical dysplasia	5 (38.5%)	8 (61.5%)	0.36
Vascular malformation	5 (55.6%)	4 (44.4%)	1
Others	20 (47.6%)	22 (52.4%)	0.36

Note: Analysis using the Fisher's exact test

Abbreviation: *, $p<0.05$; PET, Positron emission tomography

Table 4: Methionine PET positive and negative for each tumor

Adult-type diffuse glioma	145 (84.3%)	27 (15.7%)	0.30
Pediatric-type diffuse high-grade glioma	19 (100%)	0	0.086
Circumscribed astrocytic glioma	12 (92.3%)	1 (7.7%)	1
Glioneural/neuronal tumor	11 (64.7%)	6 (35.3%)	0.018*
Ependymal tumor	6 (75.0%)	2 (25.0%)	0.31
Germ cell tumor	5 (71.4%)	2 (28.6%)	0.25
Embryonal tumor	3 (100%)	0	1
Meningioma	11 (100%)	0	0.6
Primary central nervous system lymphoma	14 (93.3%)	1 (6.7%)	0.70
Metastatic tumor	12 (100%)	0	0.38

Others	11 (91.7%)	1 (8.3%)	1

Note: Analysis using the Fisher's exact test

Abbreviation: *, $p<0.05$; PET, Positron emission tomography

CONCLUSIONS

In conclusion, this single-center study, which included a large number of cases, provides valuable insights into tumor diagnosis using MET–PET scanning. The identification of tumors without MET uptake, along with the recognition of MET uptake in non-tumorous lesions, highlights the sensitivity and specificity limitations of PET scans. These findings emphasize the need for a multifaceted diagnostic approach that combines MET–PET with other imaging modalities and diagnostic techniques. This study serves as a foundation for future research, demonstrating the importance of developing integrated diagnostic protocols to improve accuracy in differentiating tumors from non-tumorous lesions. Further multi-center studies and exploration of complementary diagnostic methods will be essential in advancing oncological diagnostics and improving patient outcomes.

REFERENCES

1. Haberbosch L, MacFarlane J, Koulouri O, Gillett D, Powlson AS, Oddy S, et al. Real-world experience with 11C-methionine positron emission tomography in the management of acromegaly. Eur J Endocrinol. 2024;190: 307–313.

2. Takei H, Shinoda J, Ikuta S, Maruyama T, Muragaki Y, Kawasaki T, et al. Usefulness of positron emission tomography for differentiating gliomas according to the 2016 World Health Organization classification of tumors of the central nervous system. J Neurosurg. 2020;133: 1010–1019.

3. Kim D, Chun J-H, Kim SH, Moon JH, Kang S-G, Chang JH, et al. Re-evaluation of the diagnostic performance of 11C-methionine PET/CT according to the 2016 WHO classification of cerebral gliomas. Eur J Nucl Med Mol Imaging. 2019;46: 1678–1684.

4. Yamaguchi S, Hirata K, Okamoto M, Shimosegawa E, Hatazawa J, Hirayama R, et al. Determination of brain tumor recurrence using 11 C-methionine positron emission tomography after radiotherapy. Cancer Sci. 2021;112: 4246–4256.

5. He Q, Zhang L, Zhang B, Shi X, Yi C, Zhang X. Diagnostic accuracy of 13N-ammonia PET, 11C-methionine PET and 18F-fluorodeoxyglucose PET: a comparative study in patients with suspected cerebral glioma. BMC Cancer. 2019;19: 332.

6. Torii K, Tsuyuguchi N, Kawabe J, Sunada I, Hara M, Shiomi S. Correlation of amino-acid uptake using methionine PET and histological classifications in various gliomas. Ann Nucl Med. 2005;19: 677–683.

7. Palanichamy K, Chakravarti A. Diagnostic and prognostic significance of methionine uptake and methionine positron emission tomography imaging in gliomas. Front Oncol. 2017;7: 257.

8. Kaneko K, Koriyama S, Tsuzuki S, Masui K, Kanasaki R, Yamamoto A, et al. Association between pretreatment 11C-methionine positron emission tomography metrics, histology, and prognosis in 125 newly diagnosed patients with adult-type diffuse glioma based on the World Health Organization 2021Classification. World Neurosurg. 2024;186: e495–e505.

9. Terakawa Y, Tsuyuguchi N, Iwai Y, Yamanaka K, Higashiyama S, Takami T, et al. Diagnostic accuracy of 11C-methionine PET for differentiation of recurrent brain tumors from radiation necrosis after radiotherapy. J Nucl Med. 2008;49: 694–699.

10. Bag AK, Wing MN, Sabin ND, Hwang SN, Armstrong GT, Han Y, et al. 11C-methionine PET for identification of pediatric high-grade glioma recurrence. J Nucl Med. 2022;63: 664–671.

11. Bakker LEH, Verstegen MJT, Ghariq E, Verbist BM, Schutte PJ, Bashari WA, et al. Implementation of functional imaging using 11C-methionine PET-CT co-registered with MRI for advanced surgical planning and decision making in prolactinoma surgery. Pituitary. 2022;25: 587–601.

12. Roessler K, Gatterbauer B, Becherer A, Paul M, Kletter K, Prayer D, et al. Surgical target selection in cerebral glioma surgery: linking methionine (MET) PET image fusion and neuronavigation. Minim Invasive Neurosurg. 2007;50: 273–280.

13. Glaudemans AWJM, Enting RH, Heesters MAAM, Dierckx RAJO, van Rheenen RWJ, Walenkamp AME, et al. Value of 11C-methionine PET in imaging brain tumours and metastases. Eur J Nucl Med Mol Imaging. 2013;40: 615–635.

14. Wang Y, Rapalino O, Heidari P, Loeffler J, Shih HA, Oh K, et al. C11 methionine PET (MET-PET) imaging of glioblastoma for detecting postoperative residual disease and response to chemoradiation therapy. Int J Radiat Oncol Biol Phys. 2018;102: 1024–1028.

15. Maya Y, Werner RA, Schütz C, Wakabayashi H, Samnick S, Lapa C, et al. 11C-methionine PET of myocardial inflammation in a rat model of experimental autoimmune myocarditis. J Nucl Med. 2016;57: 1985–1990.

16. Tarkkonen A, Rissanen E, Tuokkola T, Airas L. Utilization of PET imaging in differential diagnostics between a tumefactive multiple sclerosis lesion and low-grade glioma. Mult Scler Relat Disord. 2016;9: 147–149.

17. Hashimoto S, Inaji M, Nariai T, Kobayashi D, Sanjo N, Yokota T, et al. Usefulness of [11C] methionine PET in the differentiation of tumefactive multiple sclerosis from high grade astrocytoma. Neurol Med Chir (Tokyo). 2019;59: 176–183.

18. Nakajima R, Kimura K, Abe K, Sakai S. 11C-methionine PET/CT findings in benign brain disease. Jpn J Radiol. 2017;35: 279–288.

19. Kubota Y, Sato T, Hozumi C, Han Q, Aoki Y, Masaki N, et al. Superiority of [11C]methionine over [18F]deoxyglucose for PET imaging of multiple cancer types due to the methionine addiction of cancer. Int J Mol Sci. 2023;24: 1935.

20. Hotta M, Minamimoto R, Miwa K. 11C-methionine-PET for differentiating recurrent brain tumor from radiation necrosis: radiomics approach with random forest classifier. Sci Rep. 2019;9: 15666.

21. Yomo S, Oguchi K. Prospective study of 11C-methionine PET for distinguishing between recurrent brain metastases and radiation necrosis: limitations of diagnostic accuracy and long-term results of salvage treatment. BMC Cancer. 2017;17: 713.

22. Louis DN, Perry A, Wesseling P, Brat DJ, Cree IA, Figarella-Branger D, et al. The 2021 WHO classification of tumors of the Central Nervous System: A summary. Neuro Oncol. 2021;23: 1231–1251.

23. Minamimoto R, Saginoya T, Kondo C, Tomura N, Ito K, Matsuo Y, et al. Differentiation of brain tumor recurrence from post-radiotherapy necrosis with 11C-methionine PET: Visual assessment versus quantitative assessment. PLoS One. 2015;10: e0132515.

24. Suzuki H, Aoki K, Chiba K, Sato Y, Shiozawa Y, Shiraishi Y, et al. Mutational landscape and clonal architecture in grade II and III gliomas. Nat Genet. 2015;47(5):458–68.

25. Aoki K, Nakamura H, Suzuki H, Matsuo K, Kataoka K, Shimamura T, et al. Prognostic relevance of genetic alterations in diffuse lower-grade gliomas. Neuro Oncol. 2018;20:66–77.

26. Aoki K, Suzuki H, Yamamoto T, et al. Mathematical modeling and mutational analysis reveal optimal therapy to prevent malignant transformation in grade II IDH-Mutant Gliomas. Cancer Res. 2021;81(18):4861–4873.

27. Ebiko Y, Tamura K, HARA S, Inaji M, Tanaka Y, Narita T, Ishii K, Maehara T, et al. T2-FLAIR mismatch sign correlates with ^{11}C-methionine uptake in lower-grade diffuse gliomas. J Neurooncol.2023;164: 257–265.

28. Verger A, Kas A, Darcourt J, Guedj E. PET imaging in neuro-oncology: An update and overview of a rapidly growing area. Cancers (Basel). 2022;14: 1103.

29. Ito K, Matsuda H, Kubota K. Imaging spectrum and pitfalls of (11)C-methionine positron emission tomography in a series of patients with intracranial lesions. Korean J Radiol. 2016;17: 424–434.

30. Tomura N, Saginoya T, Kaneko C. 18 F-fluorodeoxy glucose and 11 C-methionine accumulation in demyelinating lesions. World J Nucl Med. 2022;21: 261–266.

31. Hutterer M, Ebner Y, Riemenschneider MJ, Willuweit A, McCoy M, Egger B, et al. Epileptic activity increases cerebral amino acid transport assessed by 18F-fluoroethyl-l-tyrosine amino acid PET: A potential brain tumor mimic. J Nucl Med. 2017; 58: 129–137.

32. Hanyu T, Nishihori M, Izumi T, Goto S, Uda K, Saito R, et al. Dural Arteriovenous Fistula Mimicking a Brain Tumor on Methionine-positron Emission Tomography: A Case Report. NMC Case Report Journal. 2022; 9: 289-294

33. Ishiguro T, Nitta M, Komori T, Maruyama T, Muragaki Y, Kawamata T, et al. Transient focal magnetic resonance imaging abnormalities after status epilepticus showed 11C-methionine uptake with positron emission tomography in a patient with cerebral cavernous malformation. World Neurosurg 2018; 114: 43-46.

34. Shekari M, Verwer EE, Yaqub M, Daamen M, Buckley C, Frisoni GB, et al. Harmonization of brain PET images in multi-center PET studies using Hoffman phantom scan. EJNMMI Phys 2023;10: 68.

35. Ogawa T, Kawai N, Miyake K, Shinomiya A, Yamamoto Y, Nishiyama Y, et al. Diagnostic value of PET/CT with 11C-methionine (MET) and 18F-fluorothymidine (FLT) in newly diagnosed glioma based on the 2016 WHO classification. EJNMMI Res. 2020;10: 44.

36. van Dijken BRJ, Ankrah AO, Stormezand GN, Dierckx RAJO, Jan van Laar P, van der Hoorn A. Prognostic value of 11C-methionine volume-based PET parameters in IDH wild type glioblastoma. PLoS One. 2022;17: e0264387.

37. Isohashi K, Shimosegawa E, Kato H, Kanai Y, Hatazawa J, et al.Optimization of [11C]methionine PET study: appropriate scan timing and effect of plasma amino acid concentrations on the SUV. *EJNMMI Res.* 2013 Apr 15;3(1):27.